Journal of Marine Science and Engineering

MDPI

Article

A New Genetic and Evolutionary Model for the Ningbo Structure in the Xihu Sag, East China Sea Shelf Basin: Insights from Seismic Interpretation and Analogue Modeling

Jiafu Yu [1], Fusheng Yu [1,2,*], Zhongyun Chen [3], Chunfeng Liu [3], Yili Qi [1], Xin Liu [1] and Chen Yang [1]

[1] College of Geosciences, China University of Petroleum (Beijing), Beijing 102249, China; yu1605123510@163.com (J.Y.)
[2] State Key Laboratory of Petroleum Resources and Engineering, China University of Petroleum (Beijing), Beijing 102249, China
[3] Shanghai Branch, CNOOC China Limited, Shanghai 200335, China
* Correspondence: fushengyu@cup.edu.cn

Abstract

The central inversion tectonic belt of the Xihu Sag is a typical inversion structural zone in the East China Sea Shelf Basin and a key target for hydrocarbon exploration. The Ningbo structure underwent five evolutionary stages—rifting, post-rift transition, depression, transpressional inversion, and regional subsidence—during which the stress regime evolved from extension to transpression-dominated strike-slip deformation. This study employs seismic interpretation, fault-throw analysis and sandbox analogue modeling to clarify its genetic mechanism and controlling factors. The results show that the fault system exhibits characteristics typical of strike-slip deformation, including high-angle master faults and well-developed flower structures. Along strike, fault throw alternates between normal and reverse displacement over short distances, forming a "dolphin effect," reflecting spatial alternation between transtensional and transpressional domains. Comparison of three experimental models demonstrates that the overlap and lateral spacing of pre-existing basement faults primarily control deformation style. Greater overlap and closer spacing promote through-going fault linkage and the formation of a principal displacement zone, generating a narrow, continuous uplift belt. A three-dimensional genetic model is established, providing a unified explanation of structural patterns, with implications for similar inversion systems.

Keywords: Xihu Sag; Ningbo structure; strike-slip model; physical modeling

Academic Editor: Markes E. Johnson

Received: 4 April 2026
Revised: 20 April 2026
Accepted: 21 April 2026
Published: 22 April 2026

1. Introduction

The East China Sea Shelf Basin is a Mesozoic–Cenozoic petroliferous basin located along the eastern continental margin of China [1,2]. Its tectonic evolution has been primarily influenced by the subduction of the Izanagi, Pacific, and Philippine Sea plates [3–5]. The basin generally trends NE and is structurally characterized by a "one uplift sandwiched between two depressions" configuration, comprising, from west to east, the western depression belt, the central uplift belt, and the eastern depression belt [6]. Owing to its unique tectonic setting, abundant hydrocarbon resources, and major strategic importance, the basin has attracted extensive attention from both domestic and international geologists and hydrocarbon explorationists [7,8].

The Xihu Sag is one of the most structurally complex regions within the East China Sea Shelf Basin, where a variety of structural styles have developed, including strike-slip structures, extensional structures, and structural transfer zones [9–11]. After more than 40 years of exploration, over 100 wells have been drilled, and proven natural gas reserves have reached several hundred billion cubic meters, demonstrating its considerable exploration potential [12,13]. Within the sag, the western slope belt and the central inversion belt are the most favorable zones for hydrocarbon accumulation. In the western slope belt, traps are relatively small and scattered, whereas the central inversion belt is characterized by larger anticlines and more extensive reservoir distribution [14], although it is also more challenging to explore. The Ningbo structure is located in the central part of the central inversion belt and represents the largest anticline developed in the sag, with an area exceeding 500 km^2 [15,16]. Clarifying its genetic mechanism and principal controlling factors is therefore of great significance for future hydrocarbon exploration.

Previous studies have investigated the formation mechanism of the Ningbo structure. Qin et al. (2019) [17] suggested that the NNE-trending faults developed in the Ningbo structure underwent three stages of evolution. In the first stage, the faults were normal faults active during deposition of the Pinghu Formation and older strata, acting as growth faults that controlled sedimentation in the sag center. In the second stage, corresponding to the Huagang Movement, the earlier normal faults experienced weak inversion, cutting downward into the lower part of the Huagang Formation but not extending upward to the palaeosurface. In the third stage, corresponding to the Longjing Movement, strong inversion occurred, during which the pre-existing fault planes were reactivated, propagated upward into the Longjing Formation, and formed anticline structures. Meanwhile, Zou et al. (2021) [18], based on seismic interpretation and numerical modeling, proposed that basement heterogeneity and pre-existing basement faults influenced the development of the central inversion belt in the Xihu Sag. Accordingly, the Ningbo structure is considered to have undergone progressive evolution under the influence of rigid basement anomalies. During the early stage of compressional inversion, anticlines were mainly small to medium in size and distributed in a scattered manner. In the later stage, under continued compressional stress, the synclinal saddles that acted as separators gradually disappeared and ultimately linked to form a single large inversion anticline belt. Zhou et al. (2024) [19] proposed that fault development in the Ningbo structure primarily occurred in three stages. First, the NE–NNE-trending master faults remained active during the extensional stage, whereas the secondary faults developed discontinuously in the N–S direction. Second, during the early stage of compressional inversion, the master faults were inverted and NWW–NW-trending accommodation faults developed. Finally, in the late stage of compressional inversion, fault activity became relatively stable. Tang et al. (2025) [20] suggested that inversion intensity and deformation characteristics vary among the southern, central, and northern segments of the Ningbo structure. They attributed these differences mainly to variations in pre-existing basement faults and to local stress concentrations caused by a highly magnetic rigid basement, which resulted in strong uplift of the central segment and drove the originally independent southern and northern segments to become uplifted as well.

In summary, most existing studies have interpreted the formation of the Ningbo structure from the perspective of early extension superimposed by later coaxial compressional inversion and have emphasized the controlling role of pre-existing basement structures and faults in its development [21]. However, this framework cannot adequately explain the genetic mechanism of the shallow NNW-trending en echelon fold structures and therefore does not allow accurate prediction of the distribution patterns of hydrocarbon traps. To address this issue, this study clarifies the strike-slip genesis and evolutionary process of the Ningbo structure from the perspectives of regional geodynamic evolution

and structural deformation characteristics. It further applies sandbox analogue modeling to comparatively analyze the genetic mechanisms of inversion structures. On this basis, a three-dimensional evolutionary model of the Ningbo structure is established, providing a theoretical framework for genetic analysis of the central inversion belt in the Xihu Sag.

2. Geological Setting

The Xihu Sag is located within the eastern depression belt of the East China Sea Shelf Basin and trends overall in a NNE direction. It is approximately 440 km long from north to south and 70–130 km wide from east to west, with a total area of approximately 59,000 km^2 [22]. To the south, it is adjacent to the Diaobei Sag, Yushan Lower Uplift, Qiantang Sag, Haijiao Uplift, Changjiang Depression, Hupijiao Uplift, and Fujiang Sag, while to the east, it borders the Diaoyu Island fold-uplift belt [6] (Figure 1a). Its formation and evolution were controlled by the regional geodynamic setting of the East China Sea Basin [23]. The Xihu Sag is dominated by Cenozoic clastic sedimentation and, from bottom to top, comprises the Paleogene Pre-Baoshi Formation, Baoshi Formation, Pinghu Formation, and Huagang Formation, followed by the Neogene Longjing Formation, Yuquan Formation, Liulang Formation, Santan Formation, and the Quaternary Donghai Group [22] (Figure 2).

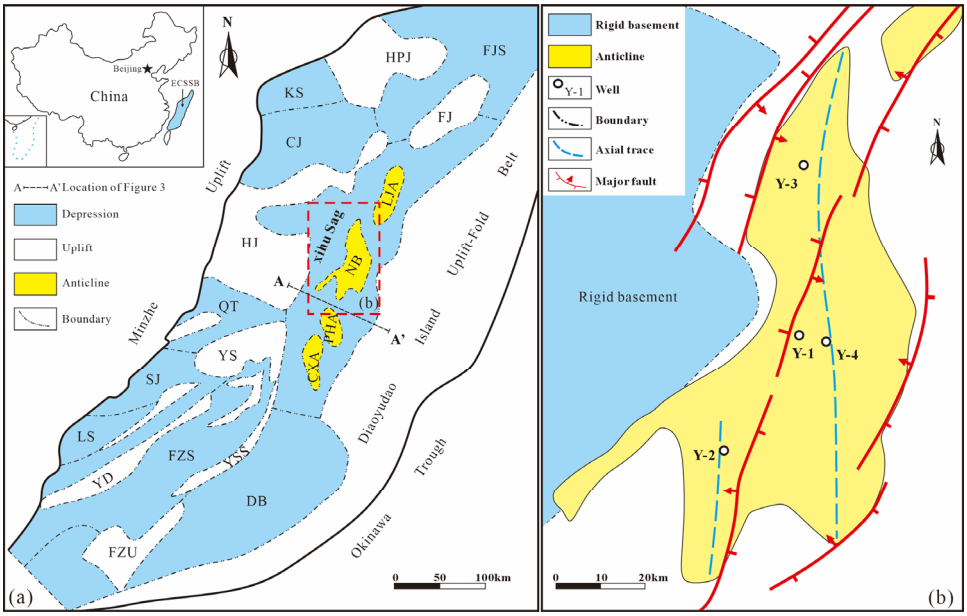

Figure 1. Tectonic framework of the East China Sea Basin and location of the Ningbo structure: (**a**) Tectonic units of the East China Sea Basin; (**b**) Regional setting of the Ningbo structure. Abbreviations of tectonic units: CJ—Changjing Sag; CXA—Chunxiao Anticline; DB—Diaobei Sag; FJ—Fujiang Uplift; FJS—Fujiang Sag; FZS—Fuzhou Sag; FZU—Fuzhou Uplift; HJ—Haijiao Uplift; HPJ—Hupijiao Uplift; KS—Kunshan Sag; LJA—Longjing Anticline; LS—Lishui Sag; NB—Ningbo Anticline; PHA—Pinghu Anticline; QT—Qiantong Sag; SJ—Shujiang Sag; YD—Yandang Uplift; YSS—Yushannan Uplift; YS—Yushan Uplift.

In plan view, the Xihu Sag is characterized by east–west zonation and north–south segmentation and can be subdivided into the western slope belt, the central depression belt, and the eastern fault-step belt [15] (Figure 1a). In vertical profile, the Paleogene strata display an east-faulted and west-overlapping half-graben geometry, whereas the Neogene strata exhibit an inverted anticline geometry [12]. The study area is located in the middle part of the central depression belt of the Xihu Sag, at the structural center of the

sag, and is characterized by a double-anticline configuration, in which the southern anticline is larger and the northern one is smaller, and the two are connected to each other (Figure 1b). The Xihu Sag experienced multiple tectonic episodes, and, based on the regional geodynamic setting and structural characteristics, its tectonic evolution can be divided into five stages: the extensional rift stage, the rift–sag transition stage, the sagging stage, the transpressional inversion stage, and the subsidence stage (Figure 3).

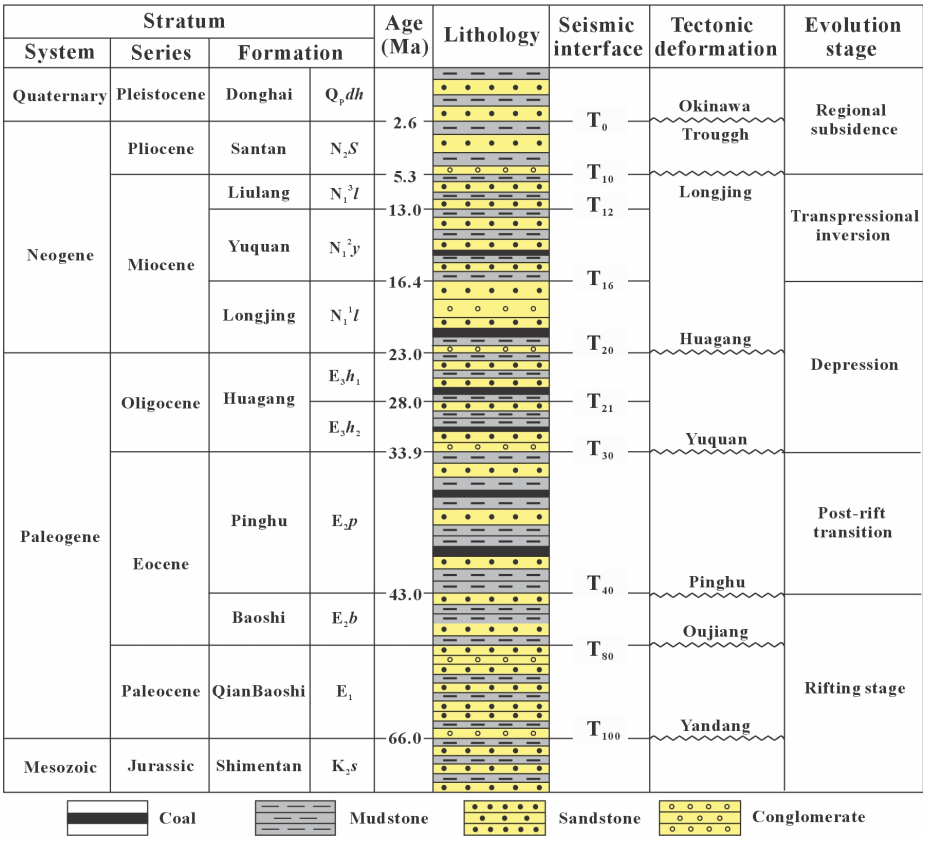

Figure 2. Generalized tectonostratigraphic column showing lithology, seismic interfaces, and tectonic evolution stages in the Xihu Sag.

Early extensional rift stage (66–43 Ma): At the initial stage of tectonic evolution, the Pacific Plate interacted with the Eurasian Plate, followed by rollback subduction of the Pacific Plate toward the NNW [5]. This process triggered the upwelling of deep material beneath the western depression belt of the East China Sea Shelf Basin, initiating its development; fault activity reached its maximum intensity during the Paleocene, and secondary faults were widely developed. Meanwhile, subduction of the Pacific Plate beneath the Eurasian Plate induced mantle flow from west to east, whereas the Indian Plate moved NNE relative to the Eurasian Plate. Under the combined influence of these factors, large-scale magmatism and strong extensional tectonism occurred along the eastern continental margin of China. The eastern depression belt of the East China Sea Shelf Basin entered an extensional rifting stage, during which boundary faults developed on both the eastern and western sides, and extensional faults also formed in the central part. During this time, the Xihu Sag was subjected to SE–NW-directed stress and began to receive sedimentation, forming strata such as the Pre-Baoshi and Baoshi formations. The strata did not undergo significant compressional folding; however, continued rifting caused partial tilting. Extensional faults developed mainly on both sides. The western side was controlled by faults of the western slope belt, characterized by relatively large throws and dominated by

extensional structural styles such as synthetic fault-step systems and grabens, thereby forming a double-fault structural pattern.

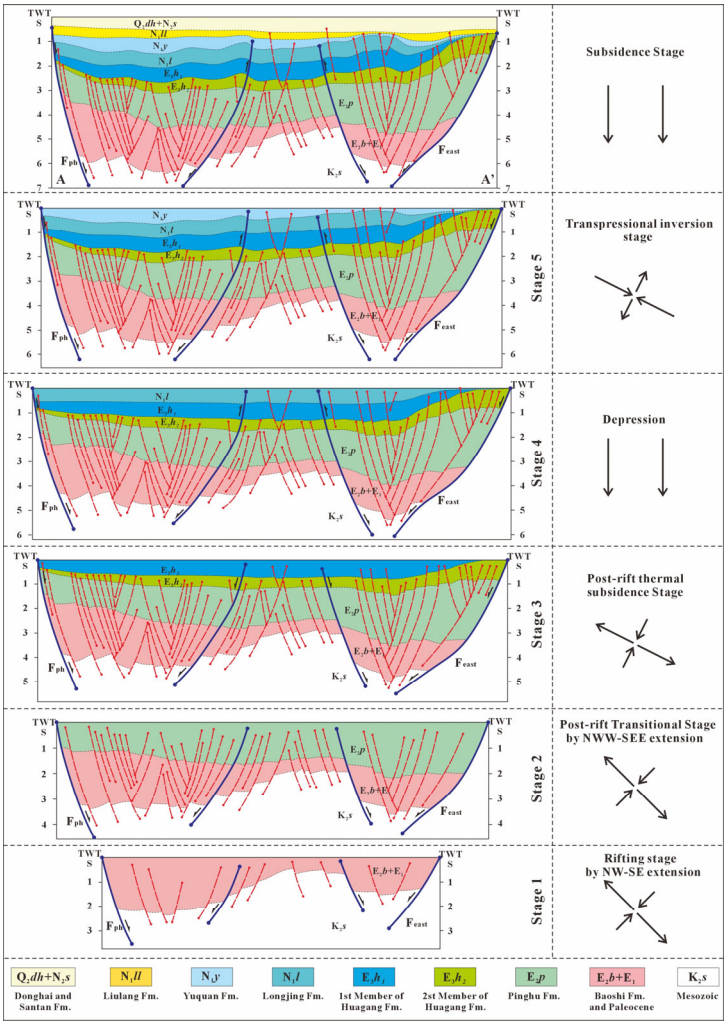

Figure 3. Sequential schematics illustrating the evolution of the Xihu Sag from the Cenozoic to the present (see Figure 1 for section locations). Arrows indicate the direction of the applied regional stress.

Post-rift transition stage (43–33.9 Ma): As time progressed, plate interaction gradually weakened, and the extensional stress acting on the Xihu Sag progressively declined. This stage corresponds to the depositional period of the Pinghu Formation. During this time, the extensional rift stage was approaching its end and transitioning into the sagging stage. Because the influence of the regional stress field on the study area was relatively weak, the strata did not undergo significant changes, whereas faults continued to develop along pre-existing fault traces.

Depression (33.9–23 Ma): During this stage, tectonic stress was relatively weak, and the strata underwent slow subsidence, during which the Huagang to Longjing formations were deposited.

Transpressional inversion stage (16.4–5.3 Ma): Interaction between the Pacific Plate and the Eurasian Plate weakened further, whereas interaction between the Philippine Sea Plate and the Eurasian Plate became increasingly significant. The Philippine Sea Plate imposed SEE–NWW-directed compressional stress on the plate boundary zone and adjacent areas, while NE-directed stress transmitted from the Indian Plate to the Eurasian Plate

also propagated into the Xihu Sag [24]. Under this complex stress regime, the central tectonic belt of the Xihu Sag underwent dextral strike-slip movement along pre-existing faults.

Regional subsidence stage (5.3 Ma to present): With continued rollback of plate subduction, the subduction rate of the Philippine Sea Plate decreased, and the strata in the Xihu Sag were characterized by regionally stable sedimentation accompanied by gradual subsidence.

3. Data and Methodology

The seismic data used in this study were collected by the CNOOC Shanghai Branch in 2022. The study area covers ~1000 km², with a vertical sampling rate of 2 ms, a dominant frequency of 25 Hz, a vertical resolution of 15–30 m, and inline and crossline spacings of 12.5 m × 25 m. Overall, the seismic data used in this study have been well collected and processed, meeting the precision requirements of this study.

Detailed interpretation of seismic profiles across the entire study area was conducted using Petrel 2021 software, on the basis of which a structural map of the top T16 horizon was compiled, and six major faults (F1–F6) were identified as the principal internal faults of the Ningbo structure. Move 2018 software was used to constrain the evolutionary stages of the Xihu Sag (Figure 3). A strike-slip structural assemblage model was established based on the map-view and cross-sectional deformation styles, together with the throw–displacement characteristics of faults F2–F4 (Figures 4–6). Physical analogue modeling was then conducted using sand layers scaled according to similarity principles (Figure 7). The specific experimental parameters are listed in Tables 1 and 2. Scan Studio software (Version: Ultra) was employed to scan the top surfaces of the experimental models to characterize their structural geometries, and the models were subsequently sliced for analysis of cross-sectional deformation styles (Figures 8–13). Based on the resulting structural evolution, deformation characteristics, and basement geometries, a three-dimensional evolutionary model of the Ningbo structure was established (Figures 14–16).

4. Evidence for the Strike-Slip Model

4.1. Plan-View Deformation Characteristics

Strike-slip faults are faults produced by relative horizontal displacement between two fault blocks under a shear stress field, and the associated deformation induced in the fault blocks or in the overlying strata during their development is collectively referred to as strike-slip tectonics [25,26]. The genetic mechanisms of strike-slip faults are generally divided into two types: pure-shear and simple-shear mechanisms. However, most strike-slip faults form under a simple-shear mechanism, as exemplified by the Tanlu fault zone and the Altyn Tagh strike-slip fault belt [27,28]. Riedel shear is currently the most widely recognized and commonly applied simple-shear genetic model for strike-slip faulting [29–31]. In the strike-slip strain ellipse of the Riedel shear model (Figure 4b), fault development is accompanied by complex structural styles, including R shears, R′ shears, T fractures, folds, normal faults, and reverse faults. In addition, combined strike-slip extension or compression may generate pull-apart basins or local uplifts.

On the present-day T16 horizon, the Ningbo structure is expressed overall as a double-anticline geometry in plan view (Figure 4a), showing clear strike-slip tectonic characteristics. The study area contains major strike-slip faults F1–F6, together with numerous secondary associated faults. Among them, F1–F6 are large in scale, highly continuous, and extend across the entire study area, exerting primary control on the overall strike and shear-deformation pattern of the fault belt, thereby forming a near-NNE-trending principal displacement zone (PDZ). The secondary faults exhibit a complete assemblage pattern

and record the progressive evolution of the shear belt from early to late stages. The R shears are arranged in right-stepping en echelon patterns in plan view and intersect the PDZ defined by F2–F4 at a small right-oblique angle of 10–20°, reflecting the principal fracture style of the early stage of shear-belt development. In general, the acute angle between an R shear and the PDZ indicates the displacement direction of the adjacent fault block, implying that the study area experienced typical dextral strike-slip movement consistent with the regional stress field. R′ shears intersect the PDZ at relatively high angles, are comparatively densely distributed, and typically terminate against R shears or the master faults, representing antithetic secondary shear fractures. P shears have a displacement direction consistent with that of the master faults and form an angle of approximately 15° with the PDZ in strike. They are less well developed in the study area and are mainly distributed around F2. In contrast to R shears, the acute angle between a P shear and the PDZ generally indicates the displacement direction of the opposite fault block. T fractures are expressed as extensional fractures or normal faults, indicating local release of tensile stress, and represent an important structural type during the late stage of shear-belt deformation. In addition, fold axial traces that obliquely intersect the PDZ are identified within the fault system. Taken together, these features indicate that the study area preserves a complete record of the progressive evolution of secondary shear structures from R to R′ to P and T, followed by progressive localization into a PDZ, and ultimately the formation of transpressional folds. Their spatial geometric characteristics are highly consistent with the classical Riedel shear model, demonstrating that fault activity in this area exhibits typical dextral strike-slip tectonic attributes.

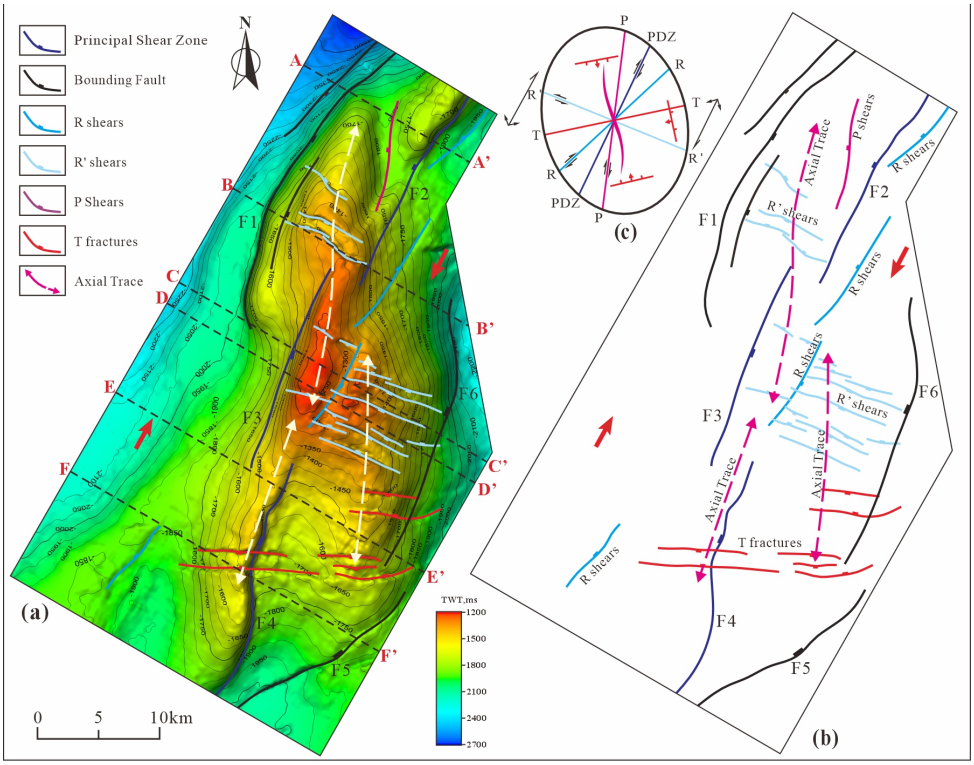

Figure 4. Plan-view structural characteristics of the T16 horizon of the Ningbo structure and the Riedel shear model: (**a**) Plan-view structural map of the T16 horizon of the Ningbo structure; (**b**) Plan-view fault distribution on the T16 horizon of the Ningbo structure; (**c**) Strike-slip strain ellipse of the Riedel shear model.

4.2. Cross-Sectional Deformation Characteristics

Layered differential deformation is clearly expressed in cross-section across the study area and can be divided into three geometries: a trough-like geometry in the deep strata of the Pinghu Formation and below, a strongly uplifted geometry in the middle strata from the Huagang to the Yuquan formations, and a gentle geometry in the shallow strata of the Liulang Formation and above. The T12 horizon, which shows clear erosion, serves as an important boundary separating the middle and shallow structural levels. Cross-sectional characteristics (Figure 5) indicate that the Ningbo structure developed under the primary control of the master faults (F1–F6), together with the coordinated influence of various secondary faults. The master fault set displays typical transpressional characteristics, including high-angle fault planes with considerable vertical extent that connect the deep and shallow levels. At depth, within the Pinghu Formation and underlying strata, the fault roots converge in a normal-fault geometry, whereas upward, they diverge within formations such as the Huagang and Longjing formations, producing Y-shaped structures and positive flower structures. Secondary faults within the flower cores and on both sides are mostly reverse faults, indicating that the strike-slip process was dominated by a compressional (thrust) component.

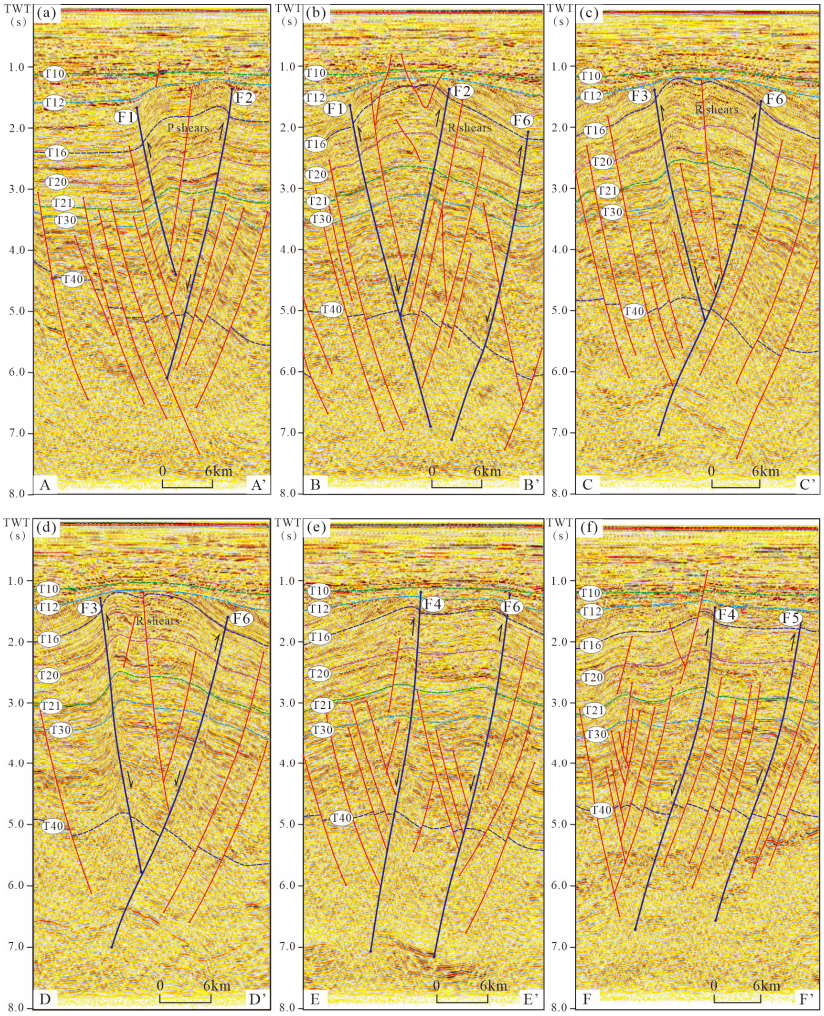

Figure 5. Deformation Characteristics of seismic sections in the study area (see Figure 4 for section locations). (**a**) The position of A-A'; (**b**) The position of B-B'; (**c**) The position of C-C'; (**d**) The position of D-D'; (**e**) The position of E-E'; (**f**) The position of F-F'.

Fault throw on both sides of the master faults exhibits a characteristic pattern of normal faulting in the lower part and reverse faulting in the upper part, together with a dolphin effect, reflecting inherited reactivation and inversion of earlier extensional structures under superposed late-stage compressional stress. At the same time, synthetic R shears or P fractures are observed on both sides of the master strike-slip faults in cross-section, locally forming push-up uplift belts and arching the shallow strata upward. These observations indicate that the fault assemblage in the study area was not controlled solely by simple compression or extension but instead formed through strike-slip deformation superimposed on, and guided by, earlier extensional structures.

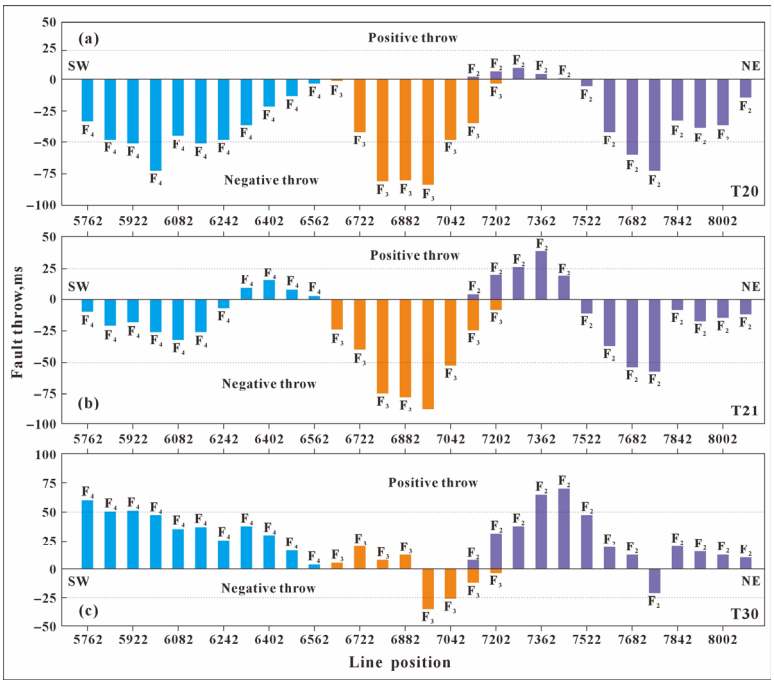

Figure 6. Along-strike throw statistics of faults F2, F3, and F4. The seismic line range in the study area is 5762–8082. Positive throw indicates normal-fault displacement, whereas negative throw indicates reverse-fault displacement. (**a**) Fault-throw statistics on horizon T20; (**b**) Fault-throw statistics on horizon T21; (**c**) Fault-throw statistics on horizon T30.

4.3. Dolphin Effect

In strike-slip fault deformation, along-strike fault throw commonly fluctuates and may undergo changes in fault sense and normal–reverse inversion over short distances. This phenomenon is referred to as the "dolphin effect" (dolphin structure effect). Statistical analysis of the along-strike fault throw of faults F2–F4 at different horizons (Figure 6) shows that F2 exhibits positive throw within the seismic line range 7122–7442 but changes to reverse throw within the range 7522–8082 (Figure 6a,b). Meanwhile, F3 shows positive throw within the seismic line range 6642–6882 but changes to reverse throw within the range 6962–7202 (Figure 6c). F4 exhibits reverse throw within the seismic line range 5762–6242 but changes to positive throw within the range 6322–6562 (Figure 6b). Along strike, fault throw thus displays an anticlinal, undulatory pattern characterized by alternating normal and reverse displacement, indicating periodic switching between releasing and restraining domains within the strike-slip belt and reflecting alternating control by stress concentration and local stress release during deformation. At the same time, the along-strike throw variations of F2–F4 show spatial and temporal offset matching. For example, within the seismic line range 7122–7282, reverse faulting on F3 develops simultaneously

with positive throw on F2, and farther east F2 transitions into a reverse fault (Figure 6a,b)). F4 gradually dies out eastward but connects well with the western end of F3, and together they form a symmetric reverse–normal–reverse pattern in throw distribution (Figure 6b). This matching relationship indicates that strike-slip displacement was transferred between adjacent faults and accompanied by local reactivation. The wavelength of the dolphin-like undulations is broadly consistent across different horizons (T30–T21–T20), whereas the positions of inversion show only minor migration. It can therefore be inferred that non-uniform partitioning of horizontal displacement along the PDZ, combined with a vertical compressional component, caused different structural segments to alternately enter uplift and subsidence states, thereby controlling the formation of the anticline structures.

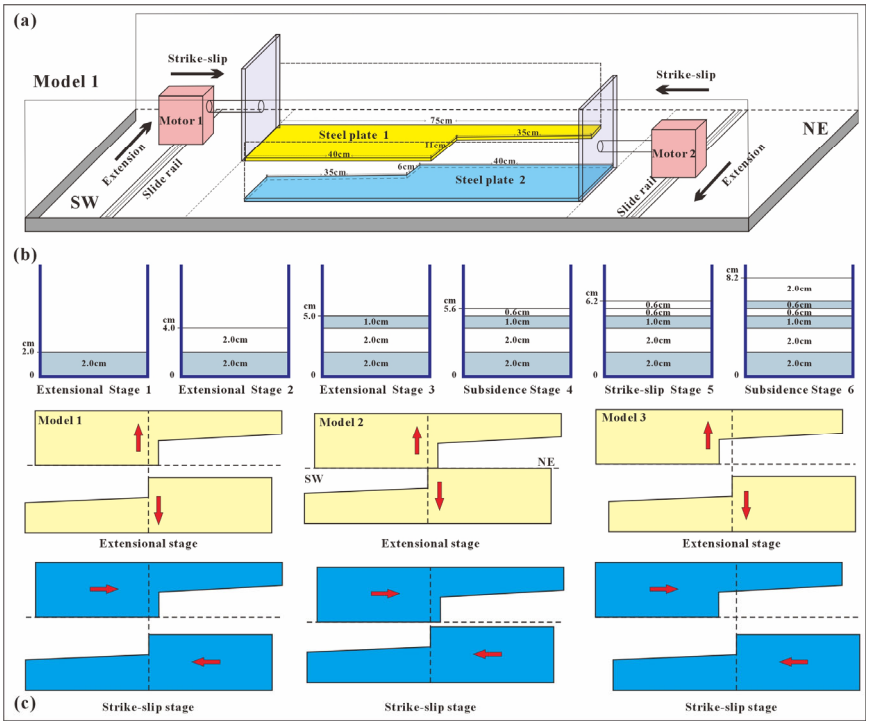

Figure 7. Geometry of the experimental apparatus and sand-layering workflow: (**a**) Three-dimensional schematic of the deformation setup used to simulate the evolution of the Ningbo structure, with principal components labeled; (**b**) Stage-by-stage sand-layering sequence for Model 1; (**c**) Basal configuration of the three model variants, showing the arrangement of the paired basement plates and their along-strike overlap and cross-strike spacing.

5. Analogue Modeling

Sandbox analogue modeling is an important approach for forward modeling of tectonic evolution, as it can reproduce brittle deformation in the shallow crust under controlled conditions and can be used to investigate its kinematic and mechanical mechanisms [32–34]. Considering that late-stage faults are commonly constrained by pre-existing structures, pre-existing basement faults were explicitly incorporated into the experiments, allowing natural boundary conditions to be more realistically approximated and their genetic significance to be better revealed [35]. Based on the above analysis of the structural deformation and evolutionary characteristics of the Ningbo structure, one reference experiment and two comparative experiments were designed in accordance with similarity principles. In these experiments, only the distribution pattern of the paired basement blocks was varied, whereas all other conditions were kept identical to simulate the

evolution of the structural belt since the Cenozoic. Comparative analysis of the experimental results can not only provide strong evidence for the genetic interpretation of the Ningbo structure but can also constrain the spatial relationship of the paired basement faults, thereby improving our understanding of the original structural configuration of the study area.

5.1. Experimental Setup and Kinematics

The experiment using Model 1 was conducted in a semi-enclosed sandbox with plan dimensions of 100 × 70 cm. The apparatus mainly consisted of sidewalls, basement steel plates, motors, and guide rails. Two basement steel plates were placed at the base of the experimental area, each measuring 75 × 30 cm. The plates were arranged as left-stepping en echelon basement faults, with an overlap of 3 cm in the NE–SW direction and a spacing of 4 cm in the NW–SE direction. These were designed to simulate pre-existing faults within the structural zone. The basement steel plates were fixed to L-shaped sidewalls, and movement along the guide rails, driven by motors, was used to simulate the extensional and strike-slip stages.

The experimental procedure was designed to be fully consistent with the tectonic evolutionary stages inferred from the natural geological model. The experiment for Model 1 was conducted in six stages. In Stage 1, a 2.0 cm thick layer of loose quartz sand was placed at the base of the model to represent the sedimentary strata of the Baoshi Formation. After a 0.02 cm thick colored quartz-sand marker layer was spread on the surface, synchronous extension in the SE–NW direction was applied over a distance of 0.4 cm. In Stage 2, another 2.0 cm thick layer of loose quartz sand was added to simulate the sedimentary strata of the Pinghu Formation. After a 0.02 cm thick colored quartz-sand marker layer was placed on the surface, synchronous extension in the SE–NW direction was again applied over a distance of 0.4 cm. In Stage 3, an additional 1.0 cm thick layer of loose quartz sand was added to simulate the sedimentary strata of the Huagang Formation. After a 0.02 cm thick colored quartz-sand marker layer was spread on the surface, synchronous extension in the SE–NW direction was applied over a distance of 0.2 cm. In Stage 4, a 0.6 cm thick layer of loose white quartz sand was placed above the deformed strata to represent the sedimentary strata of the Longjing Formation, and a 0.02 cm thick colored quartz-sand marker layer was spread on its surface. In Stage 5, another 0.6 cm thick layer of loose white quartz sand was placed above the deformed strata to represent the sedimentary strata of the Yuquan Formation, and a 0.02 cm thick colored quartz-sand marker layer was spread on the surface. A dextral strike-slip process along a NE trend was then imposed, with a total displacement of 15 cm. Finally, in Stage 6, after simulating erosion of the deformed strata, a 2.0 cm thick layer of loose white quartz sand was deposited to represent freely subsiding sedimentary strata, including the Liulang Formation, following erosion of the top surface of the Yuquan Formation. All design parameters are listed in Table 1.

The main purpose of Models 2 and 3 was to determine the basement configuration of the Ningbo structure by comparing the different anticline geometries produced by varying spatial arrangements of pre-existing faults during strike-slip deformation. Therefore, only five experimental stages were carried out, which were the same as those of Model 1. The difference is that, in Model 2, the paired basement plates overlap by 3 cm in the NE–SW direction and have 0 cm spacing in the NW–SE direction. In Model 3, the paired basement plates are separated by 3 cm in the NE–SW direction and by 4 cm in the NW–SE direction. After completion of the experiment, the top surface was scanned and modelled. A 2 cm thick sand layer was then spread to cover the model and uniformly sprayed with water. The model was left undisturbed for one day to preserve the internal deformation

within the sandbox, after which it was cut at equal intervals, and representative sections were interpreted and analyzed. All design parameters are listed in Table 1.

Table 1. Kinematic settings for structural analogue modeling.

Deformation Stage			Moving Types	Direction	Total Amount, cm	Total Model Thickness, cm
Model 1	Model 2	Model 3				
1	1	1	Extension	NW-SE	0.4	2.0
2	2	2	Extension	NW-SE	0.4	4.0
3	3	3	Extension	NW-SE	0.2	5.0
4	4	4	Subsidence			5.6
5	5	5	Strike-slip	NE-SW	15	6.2
6			Subsidence after denudation			8.2

5.2. Scaling

The overall length, width, and height of the model were designed at a geometric scale of 1:10,000, and the thicknesses of the sand layers in the experiments were arranged according to the same similarity ratio (Figure 7), such that 1 cm in the model represents 1 km of sedimentary strata in nature. In this study, dry quartz sand with a density of 2.3 g/cm^3, an internal friction angle of 37°, and an internal friction coefficient of approximately 0.74 was used to simulate brittle processes such as fracturing and slip in sedimentary strata under stress. According to the Coulomb failure criterion, this material is suitable for modeling deformation of brittle sediments in the upper crust [36,37]. Therefore, the similar material properties ensure that the sandbox experiments approximate the real geological processes. The detailed sand-layering sequence of the model is shown in Figure 8, and all scaling parameters used in the models are listed in Table 2.

Table 2. Scale parameters of structural analogue modeling.

Scaling Parameter	Model	Nature	Model/Nature Ratio
Length l, m	0.01	1000	1×10^{-5}
Density of sand ϱ, kg/m^3	2300	2700	0.85
Gravitational acceleration g, m/s^2	9.81	9.81	1
Friction angle, °	37	40	0.925
Internal friction μ	0.74	0.84	0.88
Cohesion τ_0, Pa	110–140	10^7	$(1.1–1.4) \times 10^{-5}$

The laboratory model and the natural prototype follow a dimensionless scaling relationship based on Cauchy kinematics, through which the natural system is scaled down to a laboratory analogue model [38]. The dimensionless scaling parameters remain constant, as expressed by

$$\sigma^* = \varrho^* \times g^* \times l^* \quad (1)$$

In this equation, the parameters σ*, ϱ*, g*, and l* represent the ratios of cohesion, density, gravitational acceleration, and length, respectively, between the experimental model and the natural geological prototype. Under normal conditions, sandbox experiments are conducted under Earth's gravity; therefore, g* = 1. In the experimental model, 1 cm corresponds to 1 km in nature, and thus the geometric similarity ratio is $l^* = 1 \times 10^{-5}$. The density of the quartz sand used in the experimental model is approximately 2.3 g/cm^3, whereas the density of the natural strata is approximately 2.7 g/cm^3; therefore, ϱ* = 0.85. Based on these values, the similarity factor is calculated as $\sigma^* = 0.85 \times 10^{-5}$.

5.3. Model Results

Under identical material properties and loading conditions, all three models exhibit a two-stage evolutionary process characterized by early extension followed by later transpressional inversion (Figures 8–13). Stages 1–3 correspond to the extensional phase (Figures 8a, 10a and 12a). Under NW–SE extensional stress, the sand layers initially developed two sets of left-stepping en echelon high-angle master boundary normal faults. Between the corresponding paired faults, a graben–horst–graben structural pattern developed successively. As a result, a narrow, elongated belt formed, which in vertical section can be interpreted as a combination of steeply dipping normal faults, corresponding to the deep graben structures observed in the cross-sectional results. In plan view, the differences are mainly expressed in two aspects: the spacing between the boundary faults and their linkage geometry. First, the spacing between the boundary faults in Models 1 and 3 is broadly similar, whereas that in Model 2 is significantly smaller. Second, Model 1 does not show an obvious fault-linkage relationship. In Model 2, boundary faults f2 and f3 are linked, showing an oppositely directed cross-linkage pattern. In Model 3, boundary faults f1 and f3 are linked, whereas f2 and f4 are close to linkage, showing a same-direction linkage pattern.

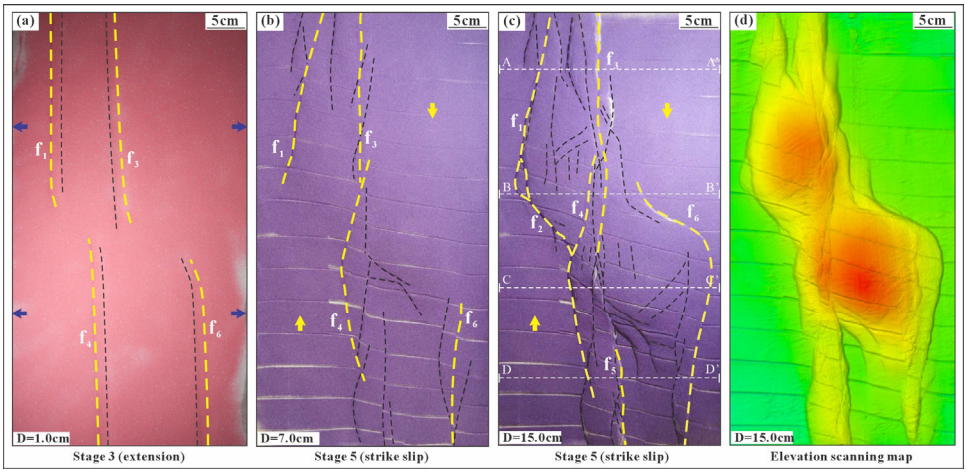

Figure 8. (**a**–**c**) Top views (photographs and line drawings) of different stages of Model 1; (**d**) Elevation scanning map; D represents displacement distance, and arrows indicate movement direction.

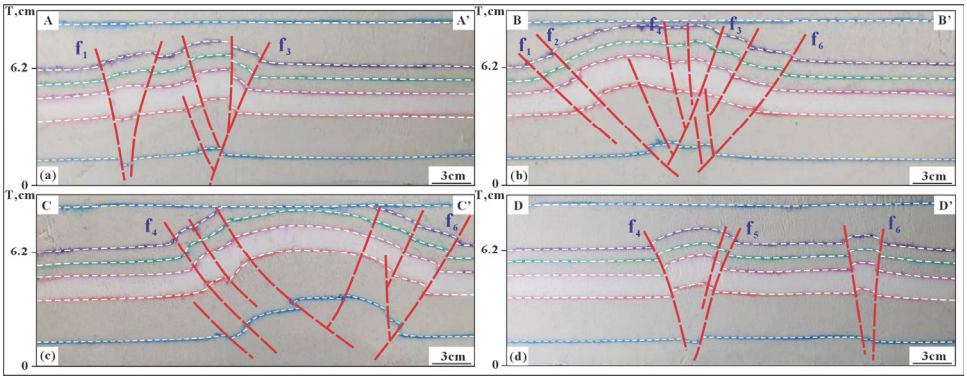

Figure 9. Cross-section interpretations (photographs and line drawings) of the final stage of Model 1, showing deformation styles (for cross-section locations, see Figure 8c). T represents the total thickness of the sand layer. (**a**) The position of A-A'; (**b**) The position of B-B'; (**c**) The position of C-C'; (**d**) The position of D-D'.

Stage 5 corresponds to the dextral transpressional phase. During the intermediate stage (Figures 8b, 10b and 12b), the early normal faults in Models 1 and 2 were first

reactivated within the central linkage zone, where R shears developed. Because both shear and compressional components were concentrated there, dextral strike-slip displacement developed in the models, resulting in a belt-like initial push-up ridge. In Model 3, an uplifted anticline first developed in the linkage segment between f1 and f3, while R shears developed around f2 and f4. During the final stage (Figures 8c, 10c and 12c), all three models developed R shears, T fractures, and a PDZ formed through progressive linkage, together with associated anticline structures under the control of the master faults. In Model 1, the early-formed anticline was segmented by an uplift belt controlled by F3 and F4, forming an anticline–uplift belt–anticline structural configuration. In Model 2, the early anticline was directly offset, forming an anticline–anticline structural geometry. Finally, in Model 3, the early anticline was segmented by f2 and f3, resulting in alternating anticline–syncline–anticline structures. Scanned top-surface models (Figures 8d, 10d and 12d) provide a clearer representation of the plan-view structural characteristics.

In cross-section (Figures 9, 11 and 13), the uplifted zones display Y-shaped and flower structures, with the overlying strata arched upward. The deep strata retain graben geometries, and, owing to the erosional treatment applied in Stage 6, clear erosion is observed in the uppermost layer of Model 1.

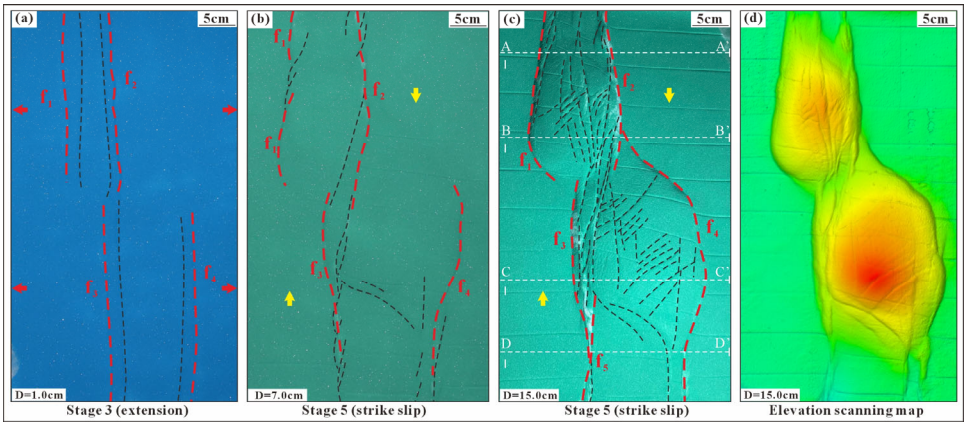

Figure 10. (**a**–**c**) Top views (photographs and line drawings) of different stages of Model 2; (**d**) Elevation scanning map; D represents displacement distance, and arrows indicate movement direction.

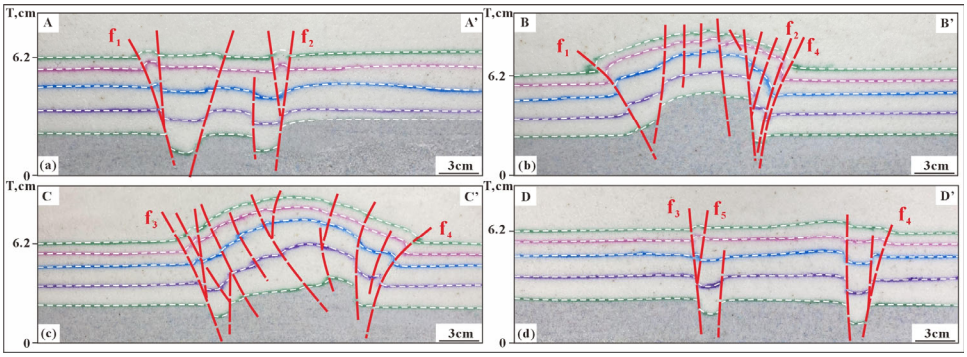

Figure 11. Cross-section interpretations (photographs and line drawings) of the final stage of Model 2, showing deformation styles (for cross-section locations, see Figure 10c). T represents the total thickness of the sand layer. (**a**) The position of A-A'; (**b**) The position of B-B'; (**c**) The position of C-C'; (**d**) The position of D-D'.

6. Discussion

6.1. Comparison Among Modeling Results

Under identical transpressional displacement, the differences among the three models are controlled solely by the spatial arrangement of the basement blocks and, based on this controlled comparison, can be reduced to two geometric parameters: the degree of overlap in the NE–SW direction and the spacing in the NW–SE direction. In Model 1, the basement blocks are arranged in an overlapping configuration with a NW–SE spacing of 4 cm. Reactivation and linkage of the boundary faults progressed gradually, and the development of through-going segments and the PDZ occurred slightly later than in Model 2, broadly in step with the elongation of the central uplift. In plan view, the central segment shows good continuity and moderate width, whereas several unlinked zones remain at both ends. In cross-section, flower structures are clearly developed.

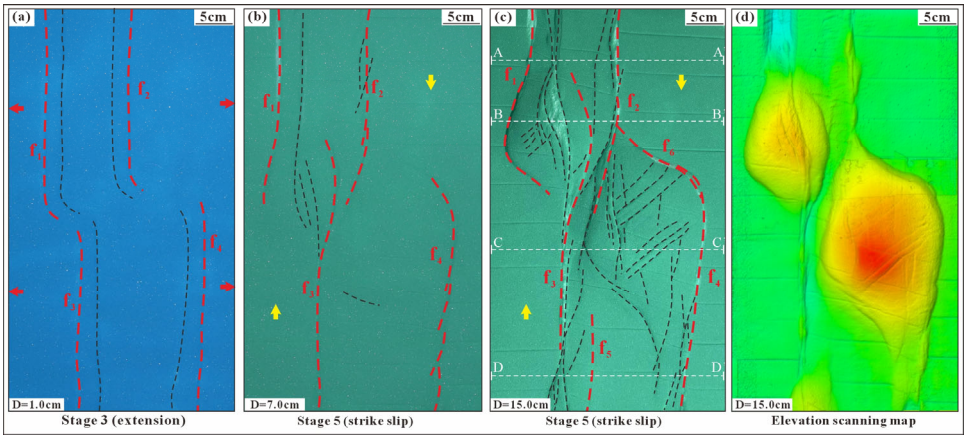

Figure 12. (**a**–**c**) Top views (photographs and line drawings) of different stages of Model 3; (**d**) Elevation scanning map; D represents displacement distance, and arrows indicate movement direction.

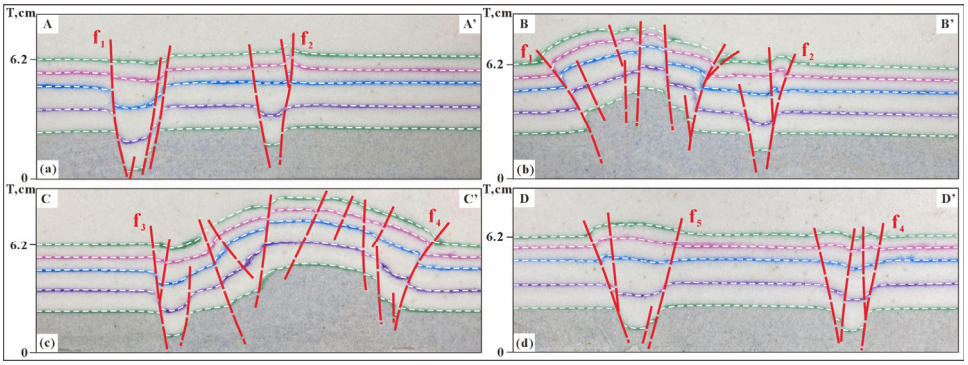

Figure 13. Cross-section interpretations (photographs and line drawings) of the final stage of Model 3, showing deformation styles (for cross-section locations, see Figure 12c). T represents the total thickness of the sand layer. (**a**) The position of A-A'; (**b**) The position of B-B'; (**c**) The position of C-C'; (**d**) The position of D-D'.

Model 2 has the same NE–SW overlap configuration as Model 1 but no spacing in the NW–SE direction. During the extensional stage, the boundary faults in Model 2 linked earlier in an opposing manner. During the strike-slip stage, the central linkage zone was the first to be reactivated, and the tips of adjacent en echelon faults linked early to form through-going strike-slip fault segments, thereby generating the PDZ at an earlier stage. In plan view, the central segment is characterized by a narrow, continuous compressional uplift belt; in cross-section, shallow and deep faults display good vertical connectivity, and flower structures are mainly concentrated in the central segment.

In Model 3, the basement blocks are arranged without overlap, but the NW–SE spacing is the same as that in Model 1 (Figures 8 and 12). During the extensional stage, the boundary faults in Model 3 linked earlier in the same direction. During the strike-slip stage, shear strain in Model 3 was not concentrated along the structural belt, the linkage zone was reactivated at a later stage, and the formation of through-going segments and/or the PDZ was delayed and limited in scale. In plan view, uplift in the central segment is discontinuous, whereas in cross-section, flower structures are poorly developed and vertical connectivity between shallow and deep faults is relatively weak.

The experimental results indicate that increased overlap promotes strain localization in the central segment, earlier fault linkage, and the development of a narrower, more continuous uplift belt. By contrast, increased lateral spacing causes deformation to become more dispersed, delays fault linkage, and results in a more discontinuous uplift pattern. These two geometric parameters therefore constitute the principal controlling factors governing differences in deformation patterns among the experiments.

6.2. Comparison Among Modeling Results and Nature

Transpressional inversion structures and positive inversion structures may display broadly similar geometries in cross-section; however, the fundamental difference lies in their stress regimes. Inversion structures are generally formed by a polarity reversal in tectonic movement, which reflects a coaxial change in the applied stress field. For example, when an extensional stress field is reversed into compressional stress acting in the same direction, the resulting structure is referred to as a positive inversion structure [39,40]. By contrast, the essential difference in the genetic mechanism between transpressional inversion and positive inversion is that, in the former, the later compressional stress is non-coaxial with the earlier extensional stress. As a result, a strike-slip component is superimposed on the original inversion deformation [41,42]. In positive inversion structures, fault strikes are generally oriented perpendicular to the principal stress direction, whereas transpressional inversion involving a strike-slip component may generate faults with a wider range of orientations, including R shears, P shears, and T fractures. These observations indicate that the shallow NWW-trending faults in the Ningbo structure, which intersect the principal faults at high angles, were formed during late-stage transpressional deformation.

The strike-slip-derived results of Model 1 were compared with the structural elements of the T16 horizon in the study area (Figure 14). The double-anticline geometry developed in Model 1 in plan view, together with the narrow fold belt in the central segment, agrees closely with the geological model. At the same time, the associated fault assemblages, including R shears, P shears, and T fractures, show a one-to-one correspondence in both fault orientation and the angle between the fold axial traces and the PDZ. These relationships are highly consistent with the Riedel shear strike-slip model. A cross-sectional comparison (Figure 15) further shows that the bidirectional double-uplift geometry and flower structures in Figure 15a, controlled by F1 and F2; the single high uplift and inverted Y-shaped and X-shaped structural styles in Figure 15b, controlled by F1, F2, and F6; the high uplift and Y-shaped structural style in Figure 15c, controlled by F3 and F6; and the single-anticline geometry and flower structures in Figure 15d, controlled in the same direction by F4 and F5, all correspond in sequence to the experimental results of Model 1 (Figure 15e–h). Importantly, the principal faults can be traced continuously from the extensional stage through to the strike-slip–transpressional stage while maintaining the same geometric control. This indicates that inversion in the study area represents reactivation of pre-existing extensional faults. When considered together with the regional geological background, independent evidence for multi-stage extension–inversion and episodic strike-slip deformation along the East China Sea margin provides a geodynamic

constraint supporting the consistency between the experiments and the natural example. Specifically, the degree of basement overlap and lateral spacing determines where strain is first localized and when the PDZ forms, thereby controlling the position and scale of anticline development. This one-to-one match validates the effectiveness of the experimental design and further indicates that the basement configuration of the study area is consistent with that of Model 1.

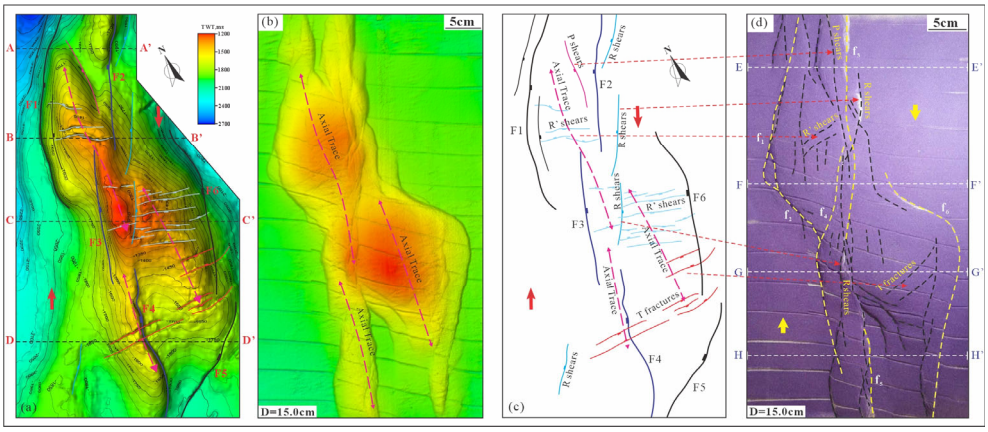

Figure 14. Comparison between the results of Model 1 and natural seismic characteristics: (**a**) Structural characteristics of the T16 horizon; (**b**) Scan image of the plan-view experimental result of Stage 5 in Experiment 1; (**c**) Fault distribution map of the T16 horizon; (**d**) Plan-view experimental result of Stage 5 in Experiment 1.

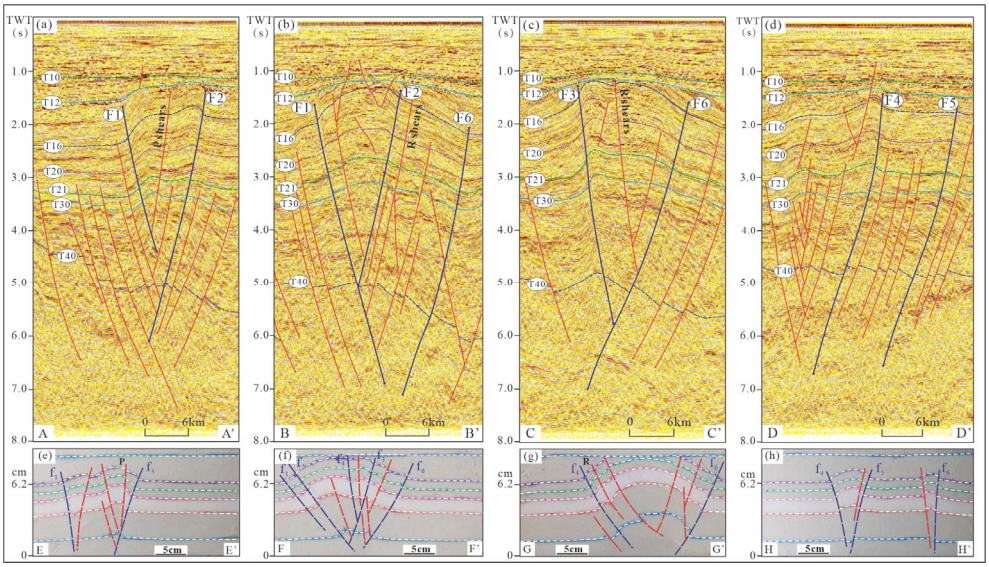

Figure 15. Comparison between the results of Model 1 and natural seismic characteristics: (**a–d**) Natural seismic section characteristics (see Figure 14a for section locations); (**e–h**) Experimental cross-sectional results of Experiment 1 (see Figure 14d for section locations).

6.3. Three-Dimensional Tectonic Evolution Model

Based on the deformation characteristics and comparison results described above, and in conjunction with the basement arrangement represented by Model 1, the evolution of the Ningbo structure can be summarized as a continuous process (Figure 16). In the early stage, a geometric framework composed of two en echelon sets of normal faults and their linkage zones provided the pre-existing fault conditions for subsequent shear

deformation. When dextral transpressional deformation was superimposed, deformation first became concentrated along the central linkage zone. The original normal faults were reactivated and underwent dextral offset, causing the tips of adjacent faults to progressively connect into through-going segments and thereby integrate into a PDZ. As the PDZ propagated along strike, the overlying strata were uplifted and bent parallel to the structural trend. The central uplift evolved from a single high point into a continuous, ridge-like structure. At the same time, synthetic shear faults cut the uplifted body, and the double anticlines were progressively established while maintaining traceable geometric consistency and vertical connectivity across different horizons. At a later stage, secondary fractures on both sides of the PDZ became distributed in belts, controlling local minor subsidence and uplift. This caused the double anticlines to exhibit rhythmic along-strike variation from continuous to discontinuous and then back to continuous. Throughout this process, the central segment remained the principal zone of displacement and uplift.

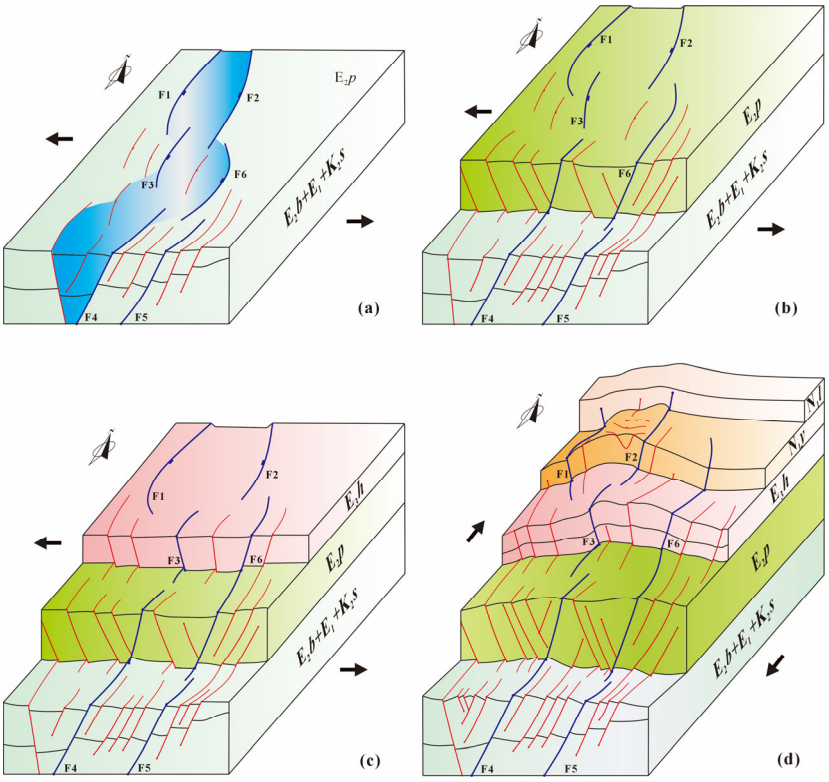

Figure 16. Tectonic evolution model of the Ningbo structure in the Xihu Sag: (**a**) rift stage; (**b**) post-rift transition stage; (**c**) depression; (**d**) strike-slip stage.

The key aspect of this model is that it integrates basement configuration, tectonic evolutionary deformation, and double-anticline geometry into a unified framework. The overlap and lateral spacing of the basement blocks jointly constrain the long-term stability and linkage style of the central segment in the study area. These factors, in turn, determine the position of the PDZ, the continuity of the uplift belt, and the geometric characteristics of the double anticlines. At the same time, the model explicitly represents the key structural elements in both map view and cross-section, including the PDZ, the arch-like uplift belt, synthetic shear faults, and the connectivity between deep and shallow faults. These elements can be matched one-to-one with the measured horizon-scale structures and cross-sectional geometries. The model therefore successfully reproduces the structural deformation and evolutionary history of the study area.

7. Conclusions

The following conclusions are drawn from a comparative analysis of the map-view and cross-sectional seismic characteristics, fault attributes, and structural analogue modeling results of the Ningbo structure in the Xihu Sag:

1. Seismic data reveal that the Ningbo structure is primarily controlled by high-angle strike-slip faults, with good vertical connectivity between deep and shallow levels in the central segment, where flower structures are commonly observed in cross-section. Along strike, fault throw exhibits an alternating normal–reverse "dolphin-like" undulatory pattern, reflecting the spatial alternation of transtensional and transpressional deformation. In spatial terms, the fault system displays a developmental sequence characteristic of strike-slip deformation, which is highly consistent with the classical Riedel shear model and indicates that fault activity in the study area exhibits typical strike-slip tectonic attributes.
2. Comparative analysis of three physical modeling experiments conducted under identical material properties and loading conditions demonstrates that the degree of overlap and the lateral spacing, as the principal parameters of basement configuration, exert the primary control on structural deformation. Increased overlap promotes strain localization in the central segment, earlier fault linkage, and the development of a narrower, more continuous uplift belt. By contrast, greater lateral spacing leads to more dispersed deformation, delayed linkage, and a more discontinuous uplift pattern. At the same time, the experimental results of Model 1 are broadly consistent with the plan-view and cross-sectional characteristics of the natural structural horizons, indicating that it represents the basement configuration that best matches the geological model.
3. The final three-dimensional evolutionary model established for the Ningbo structure provides a unified explanation for the coupling between plan-view and cross-sectional structural patterns, as well as for the associated fault characteristics. It reproduces the process whereby two sets of en echelon normal faults and their linkage zones were first formed during the extensional stage. Subsequent dextral transpression caused inherited fault reactivation and dextral offset. The linkage zones were progressively transformed into through-going strike-slip fault segments, which were integrated into a PDZ. This process ultimately produced a narrow, continuous uplift belt together with the double-anticline structure. It therefore confirms that the study area experienced a two-stage evolutionary history characterized by early extension followed by later strike-slip deformation.

Author Contributions: Conceptualization, J.Y. and F.Y.; methodology, J.Y., F.Y. and Z.C.; software, J.Y., F.Y., C.L. and Y.Q.; validation, J.Y., F.Y. and C.L.; formal analysis, J.Y., Z.C. and X.L.; investigation, J.Y., Y.Q. and C.Y.; resources, J.Y., F.Y. and Z.C.; data curation, J.Y., Y.Q., X.L. and C.Y.; writing—original draft preparation, J.Y.; writing—review and editing, J.Y., F.Y. and Z.C.; supervision, F.Y.; project administration, J.Y., F.Y. and Z.C.; funding acquisition, F.Y. and Z.C. All authors have read and agreed to the published version of the manuscript.

Funding: This work was supported by the Project of CNOOC China Limited, Shanghai Branch (CCL2023XHPS003EM). The authors declare that this study received funding from CNOOC China Limited, Shanghai Branch. The funder was not involved in the study design, collection, analysis, interpretation of data, the writing of this article, or the decision to submit it for publication.

Data Availability Statement: The data presented in this study are available on request from the corresponding author due to laboratory confidentiality regulations.

Conflicts of Interest: Authors Zhongyun Chen and Chunfeng Liu were employed by CNOOC China Limited, Shanghai Branch. The remaining authors declare that they have no known competing financial interests or personal relationships that could have appeared to influence the work reported in this paper. All authors have read and agreed to the published version of the manuscript.

References

1. Dai, L.M.; Li, S.Z.; Lou, D.; Liu, X.; Suo, Y.H.; Yu, S. Numerical modeling of Late Miocene tectonic inversion in the Xihu Sag, East China Sea Shelf Basin, China. *J. Asian Earth Sci.* **2014**, *86*, 25–37.
2. Liu, Y.M.; Hao, F.; Wu, Z.P.; Liu, L.J.; Du, Q.Z. Characteristics and origin of rift migration within the East China Sea Basin: Coupling relation with deep mantle dynamics. *J. Struct. Geol.* **2025**, *191*, 105334.
3. Hall, R. Late Jurassic–Cenozoic reconstructions of the Indonesian region and the Indian Ocean. *Tectonophysics* **2012**, *570–571*, 1–41.
4. Seton, M.; Müller, R.D.; Zahirovic, S.; Gaina, C.; Torsvik, T.; Shephard, G.; Talsma, A.; Gurnis, M.; Turner, M.; Maus, S.; et al. Global continental and ocean basin reconstructions since 200 Ma. *Earth-Sci. Rev.* **2012**, *113*, 212–270.
5. Li, S.Z.; Suo, Y.H.; Li, X.Y.; Liu, B.; Dai, L.M.; Wang, G.Z.; Zhou, J.; Li, Y.; Liu, Y.M.; Cao, X.Z.; et al. Microplate tectonics: New insights from micro-blocks in the global oceans, continental margins and deep mantle. *Earth-Sci. Rev.* **2018**, *185*, 1029–1064.
6. Zhu, W.L.; Zhong, K.; Fu, X.W.; Chen, C.F.; Zhang, M.Q.; Gao, S.L. The formation and evolution of the East China Sea Shelf Basin: A new view. *Earth-Sci. Rev.* **2019**, *190*, 89–111.
7. Tian, A.Q.; Liu, C.L.; Liu, C.X.; Huang, D.W.; Huo, H.L.; Liu, B.B.; Gao, H.Y.; Tian, Z.Y. Origin of the Cenozoic faults in the "B" structure of the central inversion belt in the northern part of the Xihu Sag, East China Sea Basin. *Mar. Pet. Geol.* **2025**, *178*, 107429.
8. Jiang, Y.M.; Tang, X.J.; Fu, X.W.; Zhong, R.Q.; Zhu, W.L. Differential geological responses and geodynamic mechanisms of major Cenozoic tectonic Movements in the East China Sea Shelf basin. *J. Asian Earth Sci.* **2025**, *284*, 106569.
9. Wang, Q.; Li, S.Z.; Guo, L.L.; Suo, Y.H.; Dai, L.M. Analogue modeling and mechanism of tectonic inversion of the Xihu Sag, East China Sea Shelf Basin. *J. Asian Earth Sci.* **2017**, *139*, 129–141.
10. Wang, F.W.; Chen, D.X.; Du, W.L.; Zeng, J.H.; Wang, Q.C.; Tian, Z.Y.; Chang, S.Y.; Jiang, M.Y. Improved method for quantitative evaluation of fault vertical sealing: A case study from the eastern Pinghu Slope Belt of the Xihu Depression, East China Sea Shelf Basin. *Mar. Pet. Geol.* **2021**, *132*, 105224.
11. Yu, J.F.; Yu, F.S.; Chen, Z.Y.; Liu, C.F.; Qi, Y.L.; Liu, X. Structural evolution characteristics and analogue modeling of the arcuate fault zone in the western slope of Xihu Sag, East China Sea shelf basin. *Chin. J. Geol.* **2026**, *61*, 606–621.
12. Xu, F.H.; Xu, G.S.; Liu, Y.; Zhang, W.; Cui, H.Y.; Wang, Y.R. Factors controlling the development of tight sandstone reservoirs in the Huagang Formation of the central inverted structural belt in Xihu sag, East China Sea Basin. *Pet. Explor. Dev.* **2020**, *47*, 101–113.
13. Wang, Y.X.; Chen, J.F.; Pang, X.Q.; Zhang, T.; Zhu, X.J.; Liu, K.X. Hydrocarbon generation and expulsion of tertiary coaly source rocks and hydrocarbon accumulation in the Xihu Sag of the East China Sea Shelf Basin, China. *J. Asian Earth Sci.* **2022**, *229*, 105170.
14. Yang, Y.Z.; Huang, Z.L.; Pan, Y.S.; Liu, C.F.; Qu, T.; Li, Z.Y. Hydrocarbon accumulation process and reservoir-forming models of structure A in the central inversion tectonic belt of the Xihu Depression, East China Sea Basin. *Nat. Gas Ind. B* **2024**, *11*, 341–356.
15. Hu, M.Y.; Li, S.Z.; Dai, L.M.; Suo, Y.H.; Guo, L.L.; Ian, S.; Liu, Z.; Ma, F.F. Dynamic mechanism of tectonic inversion and implications for oil-gas accumulation in the Xihu Sag, East China Sea Shelf Basin: Insights from numerical modeling. *Geol. J.* **2017**, *53*, 225–239.
16. Cheng, Y.J.; Wu, Z.P.; Xu, B.; Zhang, J.; Chu, Y.C.; Dai, Y.N.; Xu, L.L.; Sun, W.J.; Ma, S. Structural characteristics and genetic mechanism of transfer zones in an extensional rift zone: An example from the xihu sag, east china sea basin. *Tectonophysics* **2023**, *856*, 229852.
17. Qin, J.; Jiang, Y.M.; Li, N.; Chang, Y.S.; Zhao, H.; Liao, K.F. Hydrocarbon accumulation process in the Structure Y of Xihu Sag, East China Sea Shelf Basin and its implications for feature exploration. *Mar. Geol. Quat. Geol.* **2019**, *39*, 159–168.
18. Zou, W.; Yu, Y.X.; Liu, J.S.; Jiang, Y.M.; Tang, X.J.; Chen, S.; Yu, L. Main controlling factors of the central inversional structure belt and the development of Ningbo anticline in Xihu sag, East China Sea Basin. *Acta Pet. Sin.* **2021**, *42*, 176–185.
19. Zhou, P.; Sun, P.; Liu, C.F.; Xiong, Z.W. On time-space matching of hydrocarbon accumulation in the Yuquan Structure, Xihu Sag. *Mar. Geol. Quat. Geol.* **2024**, *44*, 121–129.

20. Tang, X.J.; Zhu, H.H.; Li, N.; Yu, Y.X.; Zhong, R.Q.; Yu, L. Segmented differential deformation of inverted anticlines and its significance on hydrocarbon accumulation in the Ningbo structural zone, Xihu Sag, East China Sea Shelf Basin. *Oil Gas Geol.* **2025**, *46*, 167–177.
21. Jiang, Y.M.; Zou, W.; Liu, J.S.; Tang, X.J.; He, X.J. Genetic Mechanism of Inversion Anticline Structure at the End of Miocene in Xihu Sag, East China Sea: A New Understanding of Basement Structure Difference. *Earth Sci.* **2020**, *45*, 968–979.
22. Wang, W.G.; Lin, C.Y.; Zhang, X.G.; Dong, C.M.; Ren, L.H.; Lin, J.L. Provenance, clastic composition and their impact on diagenesis: A case study of the Oligocene sandstone in the Xihu sag, East China Sea Basin. *Mar. Pet. Geol.* **2021**, *126*, 104890.
23. Li, C.F.; Zhou, Z.Y.; Ge, H.P.; Mao, Y.X. Rifting process of the Xihu Depression, East China Sea Basin. *Tectonophysics* **2009**, *472*, 135–147.
24. Ren, J.Y.; Tamaki, K.; Li, S.T.; Zhang, J.X. Late Mesozoic and Cenozoic rifting and its dynamic setting in Eastern China and adjacent areas. *Tectonophysics* **2002**, *344*, 175–205.
25. Peng, Z.Y.; Graveleau, F.; Bruno, C.; Vendeville, B.C.; Wang, X.; Averbuch, O. Interaction between basement inherited strike-slip structures and thrust wedge propagation in the northern Tianshan foreland basin: Insight from analogue modeling experiments. *J. Struct. Geol.* **2024**, *183*, 105143.
26. Ma, B.S.; He, Y.; Chen, L.X.; Wu, G.H.; Dong, H.Q.; Wang, J.; Yao, J.; Liu, X.C. Linkage, evolution and formation mechanism of the partially-thoroughgoing intra-cratonic conjugate strike-slip fault system in the northern Tarim Basin, NW China. *J. Asian Earth Sci.* **2025**, *294*, 106784.
27. Zuza, A.V.; Yin, A.; Lin, J.; Sun, M. Spacing and strength of active continental strike-slip faults. *Earth Planet. Sci. Lett.* **2017**, *457*, 49–62.
28. Sun, Y.J.; Wang, H.B.; Huang, Y.; Wang, J.F.; Jiang, H.L.; He, Y.C.; Huang, Z.C. Insight into seismotectonics of the central-south Tanlu Fault in East China from P-wave tomography. *J. Asian Earth Sci.* **2023**, *258*, 105722.
29. Sylvester, A.G.; Smith, R.R. Tectonic transpression and basement-controlled deformation in San Andreas fault zone, Salton trough, California. *AAPG Bull.* **1976**, *60*, 2089–2101.
30. Venncio, M.B.; Silva, F.C.A.D. Structures evolution along strike-slip fault zones: The role of rheology revealed by PIV analysis of analog modeling. *Tectonophysics* **2023**, *851*, 229764.
31. Zhu, M.J.; Wang, G.Z.; Li, S.Z.; Liu, Y.J.; Wang, P.C.; Guo, L.L.; Zhao, L.; Chen, X.P.; Song, T.H. An overview of structures associated with bends of strike-slip faults: Focus on analogue and numerical models. *Mar. Pet. Geol.* **2024**, *167*, 106983.
32. Deng, H.L.; Koyi, H.A.; Froitzheim, N. Modeling two sequential coaxial phases of shortening in a foreland thrust belt. *J. Struct. Geol.* **2014**, *66*, 400–415.
33. Yu, F.S.; Koyi, H. Cenozoic tectonic model of the Bohai Bay basin in China. *Geol. Mag.* **2016**, *153*, 866–886.
34. He, W.G.; Yu, Y.X.; Luo, Y.; Li, S.G. Effects of friction properties and rheological structures on the deformation patterns and evolution of fold-and-thrust belts-New insights from analogue modeling. *J. Struct. Geol.* **2023**, *173*, 104904.
35. Ventisette, C.D.; Bonini, M.; Maestrelli, D.; Sani, F.; Iavarone, E.; Montanari, D. 3D-thrust fault pattern control on negative inversion: An analogue modeling perspective on central Italy. *J. Struct. Geol.* **2020**, *143*, 104254.
36. Koyi, H.A.; Vendeville, B.C. The effect of décollement dip on geometry and kinematics of model accretionary wedge. *J. Struct. Geol.* **2003**, *25*, 1445–1450.
37. Rojo, L.A.; Koyi, H.; Cardozo, N.; Escalona, A. Salt tectonics in salt-bearing rift basins: Progradational loading vs. extension. *J. Struct. Geol.* **2020**, *141*, 104193.
38. Wang, Y.H.; Yu, F.S.; Zhao, B.Y.; Meng, L.J. New model of linkage evolution for the transtensional fault systems in the Nanpu Sag of Bohai Bay Basin:Insight from seismic interpretation and analogue modeling. *Pet. Sci.* **2024**, *21*, 2287–2310.
39. Scisciani, V.; Agostini, S.; Calamita, F.; Pace, P.; Cilli, A.; Giori, I.; Paltrinieri, W. Positive inversion tectonics in foreland fold-and-thrust belts: A reappraisal of the Umbria–Marche Northern Apennines (Central Italy) by integrating geological and geophysical data. *Tectonophysics* **2014**, *637*, 218–237.
40. López, C.; Cisternas, R.; Espinoza, S.; González, R.; Martínez, F.; Riquelme, R.; Montenegro, D.; Morales, J. The effects of positive tectonic inversion structures on the formation of thrust systems on the western Domeyko Cordillera, northern Chile: Implications for the orogenic development of the outer Andean forearc. *J. S. Am. Earth Sci.* **2023**, *127*, 104376.
41. Quintana, L.; Alonso, J.L.; Pulgar, J.A.; Roberto, L.; Fernández, R. Transpressional inversion in an extensional transfer zone (the Saltacaballos fault, northern Spain). *J. Struct. Geol.* **2006**, *428*, 2038–2048.
42. Kwak, Y.; Park, S.; Park, C.; Song, Y.; Smeraglia, L. Mesozoic transpressional structural inversion and synkinematic crustal fluid circulation around the northeastern Chungnam basin, southwestern Korean Peninsula: Tectonic implications. *J. Struct. Geol.* **2024**, *180*, 105070.

https://doi.org/10.3390/jmse14090764